DESIGN AND EXPERIMENTAL IMPLEMENTATION OF AN AUTOMATED HELIOSTAT SYSTEM FOR SOLAR HEAT FOR INDUSTRIAL PROCESSES

Jesús Gabriel Silva-Morales[1], Héctor Daniel García-Lara[1], Abraham Andrade-Puente[1], José Dhair Arredondo-Hernandez[1] and Job Ordaz-Castillo[1]

[1] *Universidad Autónoma de Nuevo León, Facultad de Ingeniería Mecánica y Eléctrica (FIME), Laboratory for Research and Innovation in Energy Technology (LIITE), Av. Universidad s/n, Ciudad Universitaria, San Nicolás de los Garza, Nuevo León, C.P. 66455, Mexico*

jesus.silvams@uanl.edu.mx, hector.garcialra@uanl.edu.mx

Summary

This study presents the design and experimental validation of a modular heliostat system to improve solar thermal concentration for industrial processes. It conducts a comparative analysis between an initial 30cm x 30cm prototype and a new 20cm x 20cm design. Both configurations were operated using a custom trigonometric control algorithm via a web interface, with empirical data cross-validated against TracePro optical simulations and NREL ephemeris data. Results indicate that the optimized 20cm x 20cm design significantly enhanced tracking precision, reducing the average angular error from 2.55° and 8.59° to 2.47° and 7.27°. Furthermore, the average azimuthal deviation decreased from 4.10° to 0.65°, and the calculated elevation error was minimized to 1.14%. The system achieved an approximate concentrated irradiance of 1.9 W/m^2, limited primarily by the cosine factor. By aligning the mirror's centroid collinearly with its rotational axes, the new design successfully mitigated mechanical tracking deviations. Future work aims to integrate camera-based shadow analysis for fully automated, closed-loop tracking.

Keywords: Concentrated Solar Power (CSP), Heliostat Field, Simulation, Experimental Validation, SHIP

Field of application for the findings: 03. Sustainable Heat for Industrial Process

Addressed audience: Academic researchers and R&D engineers interested in the evolution of renewable energy technologies

1. Introduction

1.1 Background and Energy Context

Globally increasing energy demand, driven by population growth and the urgency to mitigate greenhouse gas emissions, has positioned concentrated solar power (CSP) as a viable and sustainable technological alternative. At the global scale, the industrial sector accounts for approximately 32-35% of total energy demand, with nearly 74% of this energy being used specifically for industrial process heat Kumar et al. (2019). This structural dependence is consistent even across regions with advanced decarbonization frameworks; recent data from Eurostat indicates that industry accounts for 23.9% of the European Union's final energy consumption. Furthermore, while renewables and biofuels constitute 11.3% of this industrial energy mix, the direct penetration of solar thermal heat remains marginal, with the sector still heavily dictated by natural gas and electricity Eurostat (2024).

In the specific context of Mexico, the industrial sector represents 32.8% of the national final energy consumption, equivalent to 1,826.95 PJ. While this sector remains heavily dominated by natural gas and electricity, there is a clear and accelerating shift toward renewable adoption. Notably, the integration of solar energy in the industrial mix experienced a significant proportional increase, growing from a mere 0.12% Secretaría de Energía (SENER)

(2023) to 1.7% (31.49 PJ) Secretaría de Energía (SENER) (2024). Despite this promising upward trend, solar thermal technologies are still vastly underutilized relative to the country's exceptional solar irradiance potential. This scenario highlights both an expanding market and an urgent need for efficient, scalable renewable heating solutions to accelerate the industrial energy transition.

1.2 Solar Heat for Industrial Processes (SHIP)

This sustainable approach is increasingly applied through Solar Heat for Industrial Processes (SHIP), a sector that reached a global thermal capacity of over 1 GWth by the end of 2024. Industrial process heat is technically classified into three primary temperature ranges: low-temperature (below 150 °C), medium-temperature (150 °C to 400 °C), and high-temperature (above 400 °C) Solar Payback (2017). Currently, the SHIP market is largely dominated by parabolic trough collectors and technologies well-suited for low- and medium-temperature applications across the food, beverage, and textile industries AEE INTEC (2026). The technical and economic viability of these systems has been successfully demonstrated in facilities like the Lechera Guadalajara dairy plant in Mexico, where a parabolic trough solar field delivers heat at 78 °C, displacing 35% of the thermal demand for milk pasteurization (Solar Payback, 2017, p. 7). Similarly, European benchmark projects in the paper industry demonstrate how solar thermal arrays Solar Heat Europe (2026), often coupled with industrial heat pumps European Heat Pump Association (EHPA) (2026), can reliably supply massive process heat loads.

However, as analyzed by Marzouk (2025), there is an anticipated shift toward more complex designs, such as solar power towers (SPTs), to address high-temperature industrial demands. These systems rely on two-axis solar tracking and point-focused concentration, a trend expected to align with large-scale deployment by 2026. Consequently, optimizing heliostat field efficiency and automation becomes essential for the continued expansion of high-temperature SHIP applications.

1.3 Related Work and State of the Art

Within these advanced SHIP systems, heliostats are critical components whose function is to capture and precisely direct incident solar radiation toward a central receiver, as described by Cock Martínez (2018). However, the widespread adoption of modular heliostat fields faces significant mechanical and control challenges. One of the primary issues in small-scale modular systems is the mechanical deviation at the center of rotation during dynamic two-axis tracking. These structural misalignments directly affect the accuracy of the mirror orientation, resulting in tracking errors that reduce the intercept factor at the target.

1.4 Research Objectives and Proposed Approach

The objective of this study is to design and experimentally implement an automated small-scale modular heliostat system for solar heat for industrial processes (SHIP) applications. This work presents a comparative analysis between an initial heliostat prototype featuring a 30cm x 30cm reflector and an optimized 20cm x 20cm design. By operating both configurations via a custom trigonometric control algorithm integrated into a web-based interface, this study utilizes optical ray-tracing simulations (TracePro) and experimental validation to demonstrate that the reduced-scale geometry improves vector alignment and structural tracking accuracy.

2. Heliostat Design and Prototype Evolution

2.1 Mechanical and Geometric Specifications

Two designs are proposed for the heliostat architecture. Both configurations utilize motorized gear drives for dual-axis tracking, dynamically adjusting the reflector to redirect incident solar radiation. The first implemented prototype features independent azimuth and elevation control, employing limit switches at the base corners to establish a mechanical reference zero point.

The initial prototype featured independent control over azimuth and elevation, relying on base-mounted contact switches to define the system's origin. This design allowed for extensive azimuthal movement but restricted the elevation axis, yielding a minimum elevation of 9° at the calibration point. A significant drawback of this configuration was the misalignment between the azimuthal axis and the physical base of 31.8%, a geometric offset that increases the risk of installation inaccuracies in an experimental testing facility.

The prototype exhibited a geometric flaw where the mirror's optical center shifted during elevation adjustments. This displacement compromises the optical performance of the heliostat, causing the reflected vector to deviate with each tracking iteration and reducing the pointing accuracy on the receiver target, see Fig. 1a. Furthermore, because the optical center maintains this radial offset across all elevation angles, the azimuthal rotation axis never intersects the mirror's centroid. This lack of collinearity induces a secondary translational displacement during azimuthal tracking, Fig. 1b.

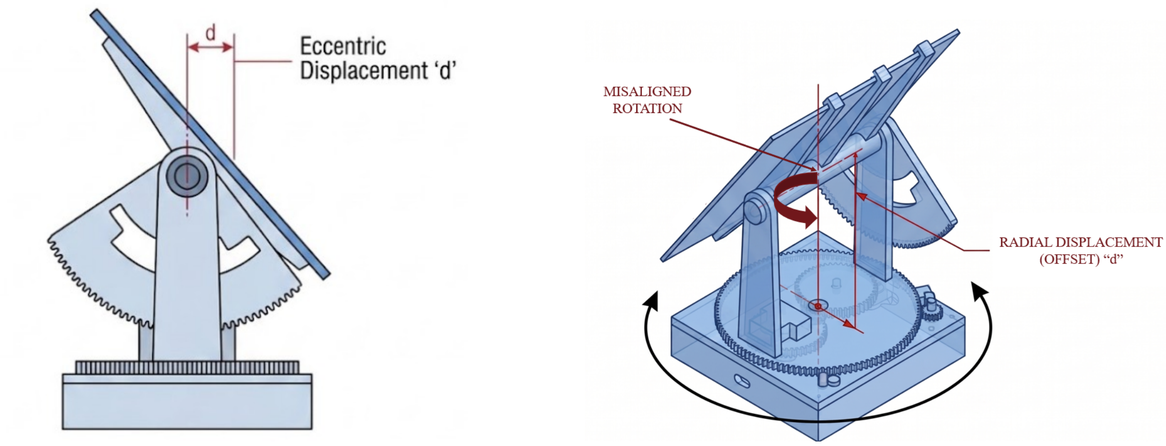

(a) Elevation dynamics of the heliostat.

(b) Rotational dynamics of the heliostat.

Fig. 1: First Design, mirror of 30cm x 30cm.

This displacement arises from a spatial offset between the reflector's optical center and the mechanical axis of rotation. Geometrically, the mirror surface acts as a tangent plane located at a radial distance from the pivot point. Consequently, during elevational adjustments, the center of the mirror traces a circular arc rather than pivoting around a stationary point.

To mitigate the kinematic deficiencies of the initial design, a second prototype was developed in which the mirror's centroid is perfectly collinear with both the azimuthal and elevational axes of rotation. This concentric alignment prevents any spatial translation of the optical vertex during tracking operations. Furthermore, precision hard stops were implemented to bound the operational range to 180° in azimuth and 90° in elevation without inducing misalignment. Ultimately, these geometric corrections minimize deviations in the reflected vector, ensuring a stable trajectory toward the concentration target independent of the instantaneous solar vector or the required tracking adjustments, see Fig. 2 for the new design.

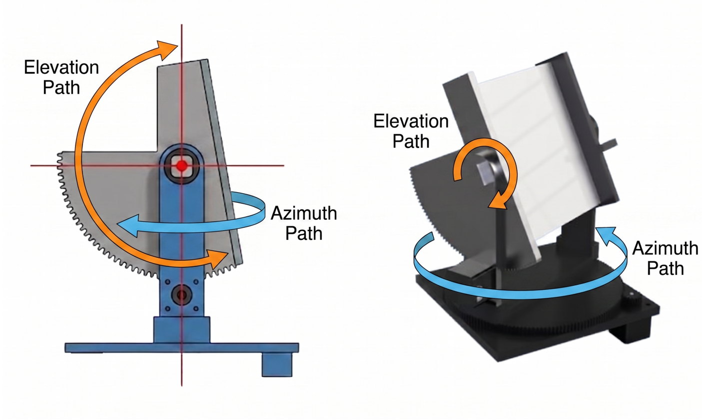

Fig. 2: Rotational dynamics of the heliostat prototype, detailing the tracking positions and the corresponding arc trajectory of the mirror center. Second design, mirror of 20cm x 20cm.

2.2 *Web Interface and Hardware Integration*

The operational control of the heliostats is driven by ESP32 microcontrollers configured in a master-slave architecture. The master node establishes a local Wi-Fi network to which the individual heliostats (slave nodes) connect. This central master is responsible for hosting the web-based interface, transmitting control commands, and monitoring the real-time operational status of each device in the network.

The web-based interface provides two operational frameworks for controlling the heliostats: an automated tracking mode (Fig. 3b) and a manual calibration mode (Fig. 3a).

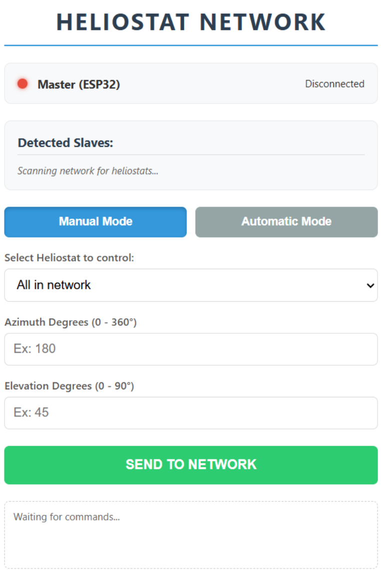

(a) Web Interface manual mode.

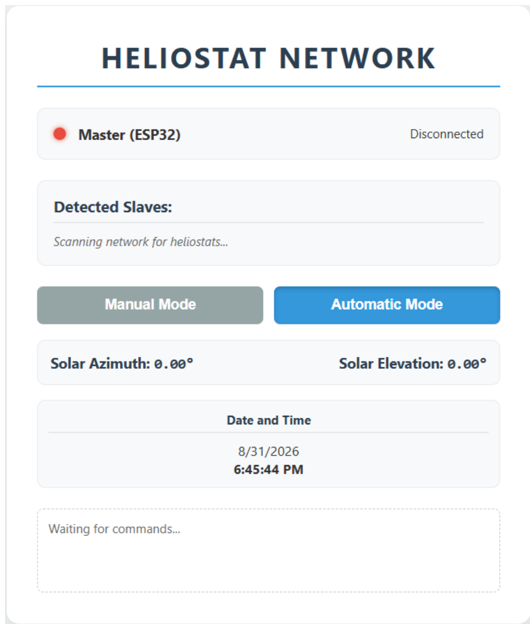

(b) Web Interface automatic mode.

Fig. 3: Web interface for the heliostats to control them manually or automatically.

3. Trigonometric Control Strategy and Solar Tracking

Autonomous heliostats employ continuous solar tracking data to achieve real-time dynamic realignment, ensuring consistent concentration. Conversely, in manually operated heliostats, mirror orientation requires iterative adjustments to ensure proper redirection toward the receiver.

This methodology assists in data acquisition and validation. In the first empirical model, elevation and azimuth parameters are manually input into the actuator controllers via a local web interface, which is initialized by each heliostat upon startup. This aligns the reflected beam with a static target, recording the precise angular coordinates required to maintain target interception over time.

The dataset derived from manual operation is validated against the solar ephemeris data provided by the National Renewable Energy Laboratory (NREL) Reda and Andreas (2004). By applying solar tracking geometry, the theoretical coordinates are transformed to align with the experimental reference frame. Subsequently, a computational simulation of the physical field is executed, where initial boundary conditions corresponding to the actual heliostat array are configured within a Python environment. Concurrently, TracePro software is utilized to conduct a rigorous ray-tracing analysis, allowing for the observation of optical behavior and the evaluation of deviations from the experimentally acquired data.

During manual operation, the system records the heliostat azimuth and elevation angles required to reflect the solar beam, along with their corresponding timestamps. This angular data defines the normal vector ($\hat{\mathbf{N}}$) of the heliostat surface, which in turn determines the direction of the reflected vector ($\hat{\mathbf{R}}$), representing the redirection of the incident solar vector ($\hat{\mathbf{S}}$) toward the target, as shown in Fig. 4.

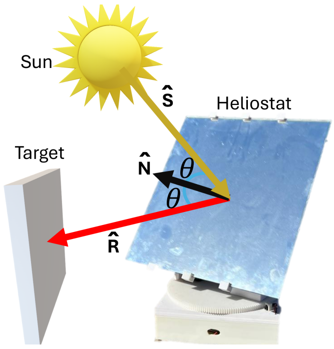

Fig. 4: Heliostat prototype and associated vector system.

The vector ($\hat{\mathbf{R}}$) is assumed to be invariant, as the target remains stationary in a fixed reference frame. Consequently, the only time-varying components are the solar vector ($\hat{\mathbf{S}}$) and the heliostats surface normal vector ($\hat{\mathbf{N}}$). Based on the manually collected samples, the instantaneous normal vector ($\hat{\mathbf{N}}$) can be derived. Concurrently, the solar vector ($\hat{\mathbf{S}}$) is retrieved from the NREL solar position algorithms for the exact timestamps associated with each measurement of ($\hat{\mathbf{N}}$).

Finally, a reflected vector $\vec{\mathbf{R}}_\mathbf{0}$ can be determined according to the law of reflection as defined in Equation 1, and afterwards the directional unit vector $\hat{\mathbf{R}}$ is calculated with Equation 2.

$$\vec{R}_0 = 2(\hat{N} \cdot (-\hat{S}))\hat{N} + \hat{S} \tag{1}$$

$$\hat{R} = \frac{\vec{R}_0}{|\vec{R}_0|} \tag{2}$$

Currently, a methodology is being implemented, based on the approach utilized by Ordaz-Castillo et al. (2026). This tool measures the solar position through shadow analysis. A camera captures the target frame, allowing for the digital processing of the cast shadow to extract the real-time solar elevation and azimuth data. These parameters are subsequently used to determine the solar vector, which is essential for calculating the mirror's normal vector and ensuring accurate radiation redirection.

4. Optical Ray-Tracing Simulation

For the optical simulation, the experimental field was modeled in TracePro, incorporating the individual heliostat mirrors and the target receiver, as illustrated in Fig. 5a, represented with only 20% of rays for visual purposes. Heliostat 2 (30cm x 30cm) and Heliostat 1 (20cm x 20cm) were both assigned a "perfect mirror" surface property. The target, measuring 42.5 x 35 cm, was configured with a "perfect absorber" front surface property. To automate the simulation, a Python script utilizing macros was developed to establish a direct interface with the software and execute the ray tracing across 14 specific time steps. This code integrates the geometric specifications of each component and reads an Excel dataset containing the corresponding times, solar azimuth, and elevation angles. A uniform irradiance of 1 W/m² was defined, simulating 1 sun per collector. Upon executing the script and analyzing the target, a peak concentration value of 1.9 suns was achieved, as depicted in Fig. 5b.

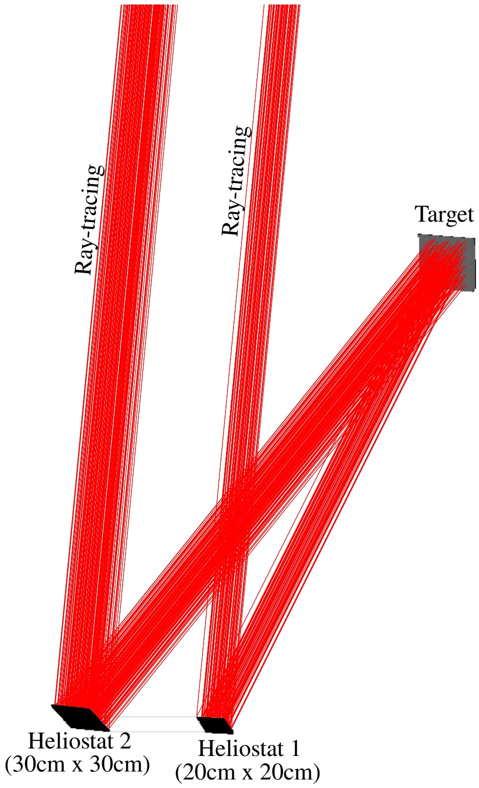

(a) TracePro simulation

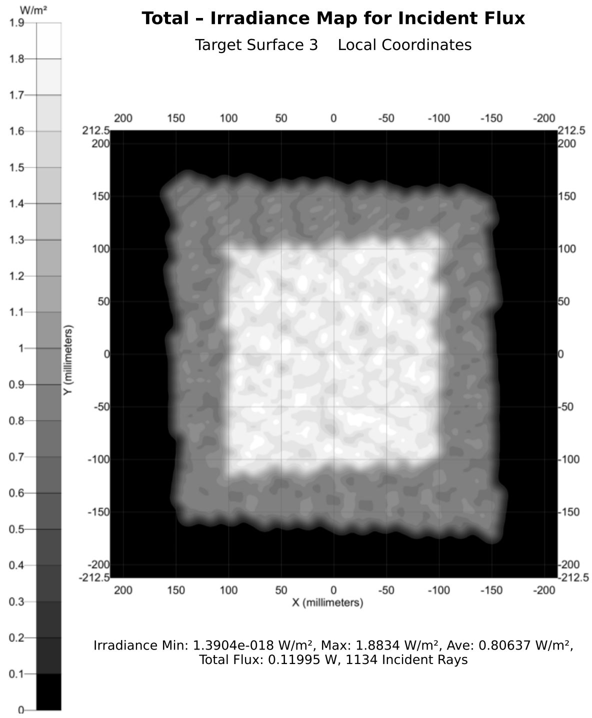

(b) TracePro irradiance map

Fig. 5: Simulated data

5. Experimental Methodology

The heliostat field was constructed on the roof of the sports center at the Facultad de Ingeniería Mecánica y Eléctrica (FIME) of the Universidad Autónoma de Nuevo León (UANL), a facility equipped for various solar collector research projects. While a 6-meter-high tower is installed on-site, a target positioned at a height of 2.5 meters was utilized for these specific experimental trials. The two heliostat prototypes were positioned 4 meters in front of the target, separated by a distance of 1 meter, as seen in Fig. 6a. Within this experimental setup, Heliostat 1 designates the optimized 20 x 20cm mirror design, while Heliostat 2 refers to the 30 x 30cm mirror used as the initial testing prototype. The difference in mirror dimensions was intended to facilitate the identification of the reflected radiation on the target during the redirection process, as shown in Fig. 6c. To experimentally quantify tracking accuracy, small reference markers were affixed to the geometric center of both the target and the individual mirrors (see Fig. 6b). Power is supplied to the heliostats via a dedicated power supply unit. Upon activation, the microcontrollers communicate with a custom web interface, which logs real-time azimuth and elevation data for each unit into an Excel file for subsequent analytical evaluation.

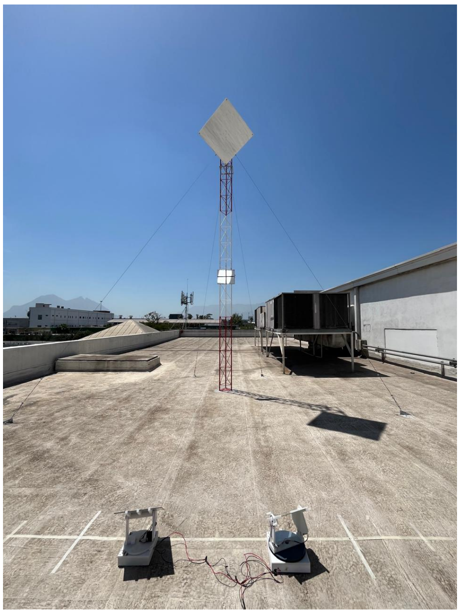

(**a**) Experimental layout

(**b**) Mirror with marker tape

(**c**) Reflection in the target

Fig. 6: Experimental setup and reference images.

6. Results

6.1 Vector Deviation Analysis

Experimental tests were carried out with the heliostat prototypes on August 22, 2026, in the municipality of San Nicolás de los Garza, Nuevo León. The test began at 11:20 hours with a sampling frequency of 10 minutes until 13:30 hours . It is worth noting that, at this initial stage of the study, the heliostats were operated electronically (in a non-autonomous manner) through a web interface. Throughout the experimentation, the rotation and inclination angles of each heliostat (γ_h, α_h) were recorded at every time step. Using this data, a vector calculation was performed in MATLAB by inputting the real variables required by the vector calculation algorithm in order to verify its operation and feasibility, as shown in Table 1 and its graphical representation of the Fig. 7.

Tab. 1: R-vector results and error percentage for heliostats.

Instant	Time	Heliostat 1 (20cm x 20cm)		Heliostat 2 (30cm x 30cm)	
		Vector R (X, Y, Z)	**Error**	**Vector R (X, Y, Z)**	**Error**
1	11:20	[0.8273, 0.1130, 0.5503]	3.10°	[0.8023, -0.0894, 0.5902]	5.60°
2	11:30	[0.8306, 0.1141, 0.5450]	2.76°	[0.7656, 0.0059, 0.6432]	11.20°
3	11:40	[0.8295, 0.1144, 0.5466]	2.87°	[0.7650, -0.0118, 0.6440]	10.70°
4	11:50	[0.8319, 0.1209, 0.5415]	2.67°	[0.7592, -0.0038, 0.6509]	11.38°
5	12:00	[0.8298, 0.1184, 0.5454]	2.86°	[0.7883, -0.0213, 0.6149]	8.60°
6	12:10	[0.8257, 0.1204, 0.5511]	3.28°	[0.8064, -0.0130, 0.5913]	7.56°
7	12:20	[0.8300, 0.1251, 0.5435]	2.91°	[0.8054, -0.0259, 0.5921]	7.13°
8	12:30	[0.8241, 0.1281, 0.5518]	3.51°	[0.7880, -0.0278, 0.6151]	8.41°
9	12:40	[0.8293, 0.1143, 0.5469]	2.89°	[0.7861, -0.0301, 0.6173]	8.49°
10	12:50	[0.8308, 0.1193, 0.5436]	2.76°	[0.7798, -0.0500, 0.6240]	8.46°
11	13:00	[0.8332, 0.1055, 0.5428]	2.52°	[0.7837, -0.0255, 0.6206]	8.82°
12	13:10	[0.8524, 0.0914, 0.5149]	0.95°	[0.7812, -0.1051, 0.6154]	7.41°
13	13:20	[0.8418, 0.0962, 0.5312]	1.76°	[0.8074, -0.0167, 0.5898]	7.35°
14	13:30	[0.8483, 0.1096, 0.5180]	0.90°	[0.8018, 0.0175, 0.5973]	9.14°
		avg	2.55°	avg	8.59°

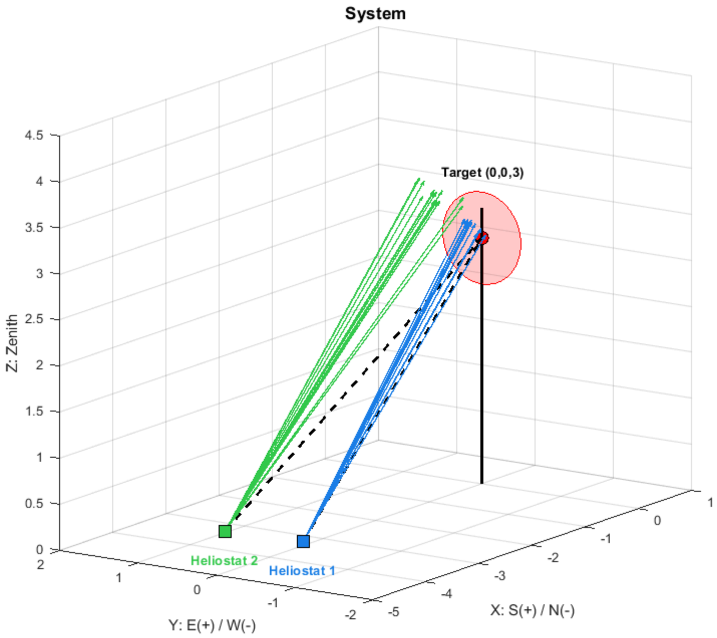

Fig. 7: Vectors from both heliostats.

6.2 Simulation vs Experimental Cross-Validation

Based on the acquired data, a simulation was conducted using TracePro and Python to recreate the experimental field conditions. Within this environment, the theoretical normal reflection vectors and the optimal angular positions required for each heliostat to project the center of the beam onto the target were calculated. The comparative results between the simulation and the experimental data are presented in Table 2.

Tab. 2: TracePro simulation vs Experimental data.

Time:	TracePro simulation				Experimental data			
	Heliostat 1		Heliostat 2		Heliostat 1		Heliostat 2	
	γ_h [°]	α_h [°]	γ_h [°]	α_h [°]	γ_h [°]	α_h [°]	γ_h [°]	α_h [°]
11:20	23.03	50.57	13.01	52.30	24	52	14.43	55
11:30	21.07	51.05	10.89	52.60	22	52.3	17.8	56.5
11:40	19.07	51.49	8.73	52.86	20	52.8	14.6	57
11:50	17.03	51.88	6.55	53.07	18.2	53	12.8	57.5
12:00	14.94	52.22	4.36	53.22	16	53.5	9.2	56.5
12:10	12.83	52.52	2.14	53.32	14	54	7.2	55.8
12:20	10.68	52.77	0.07	53.37	12	54	4.2	56
12:30	8.51	52.96	-2.29	53.37	10	54.5	1.8	56.9
12:40	6.32	53.11	-4.51	53.32	7	54.5	-0.7	57
12:50	4.11	53.21	-6.71	53.21	5	54.5	-4.2	57.2
13:00	1.89	53.25	-8.91	53.05	2	54.5	-5.2	57
13:10	0.31	53.24	-11.08	52.84	-1	53.5	-11.9	56.5
13:20	-2.53	53.18	-13.22	52.59	-3	54	-9.2	55.6
13:30	-4.73	53.06	-15.34	52.28	-4.5	53.5	-9.7	55.8

To evaluate the pointing accuracy and kinematic behavior of the prototypes, the angular error in azimuth ($\Delta\gamma$) are defined according to Equation 3.

$$\Delta\gamma = \gamma_{Exp} - \gamma_{Sim} \tag{3}$$

Where, γ_{Exp} is the experimental and γ_{Sim} is the simulated. Subsequently, the average of the angular errors was calculated, and an azimuth correction factor was defined for both heliostats according to Equation 4. This corrected value is utilized to compensate for the mechanical deviations observed during experimentation, the results of which are detailed in Table 4.

$$\gamma_h^* = \gamma_{Exp} - \Delta\gamma_{AVG} \tag{4}$$

Where γ_h^* is the corrected azimuth, γ_{Exp} is the experimental heliostat azimuth, and $\Delta\gamma_{\text{AVG}}$ is the average heliostat azimuth.

Tab. 3: ΔAzimuth and Corrected azimuth.

ΔHeliostat 1		ΔHeliostat 2		Heliostat 1	Heliostat 2
γ_{Exp}	$\Delta\gamma$	γ_{Exp}	$\Delta\gamma$	γ_h^*	γ_h^*
24	0.96	14.43	1.42	23.35	10.33
22	0.92	17.8	6.90	21.35	13.70
20	0.92	14.6	5.86	19.35	10.50
18.2	1.16	12.8	6.24	17.55	8.70
16	1.05	9.2	4.83	15.35	5.10
14	1.16	7.2	5.05	13.35	3.10
12	1.31	4.2	4.12	11.35	0.10
10	1.48	1.8	4.09	9.35	-2.30
7	0.67	-0.7	3.81	6.35	-4.80
5	0.88	-4.2	2.51	4.35	-8.30
2	0.10	-5.2	3.71	1.35	-9.30
-1	-1.31	-11.9	-0.81	-1.65	-16.00
-3	-0.46	-9.2	4.02	-3.65	-13.30
-4.5	0.23	-9.7	5.64	-5.15	-13.80
$\Delta\gamma_{AVG}$ =	0.65	$\Delta\gamma_{AVG}$ =	4.10		

It is worth mentioning that the average error in the calculated elevation was 1.14% for heliostat 1 and 3.49% for heliostat 2, one more piece of data that demonstrates the improvement in angular precision of the new design.

To analyze the angular behavior over time, graphs were plotted for both azimuth and elevation (Figs. 8-9). These graphs illustrate that by applying the correction factor, the curve aligns more closely with the simulated data. This demonstrates an angular error in the experimental measurements, which is likely associated with a misalignment from the reference axis.

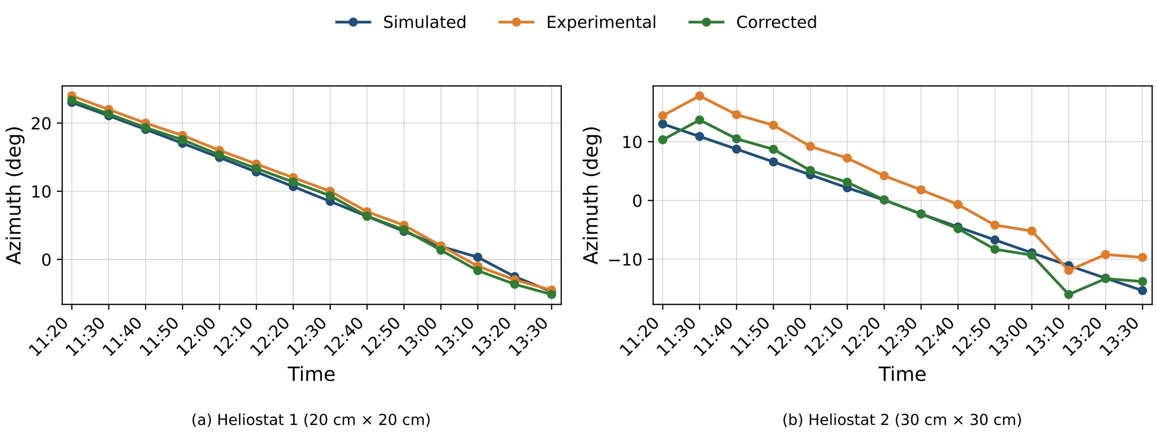

Fig. 8: Azimuth angle comparison for (a) Heliostat 1 (20cm x 20cm) and (b) Heliostat 2 (30cm x 30cm).

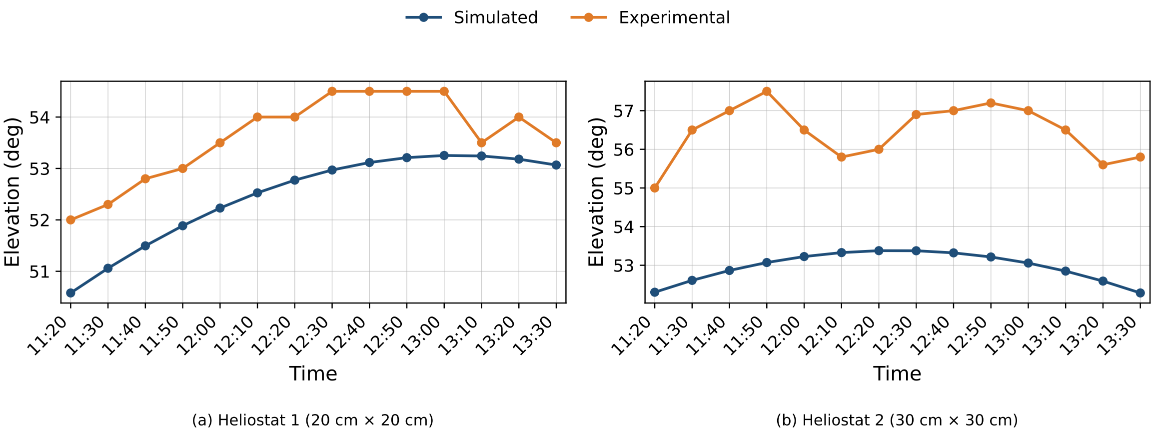

Fig. 9: Elevation angle comparison for (a) Heliostat 1 (20cm x 20cm) and (b) Heliostat 2 (30cm x 30cm).

Following the azimuth correction, the resulting vector ($\hat{\mathbf{R}}$) was recalculated and compared again with the theoretical reference vector, following the same procedure described previously. The experimental rotation and inclination angles of each heliostat were used as inputs to the vector calculation algorithm in MATLAB. This second comparison allowed the effect of the azimuth correction on the resulting vector to be evaluated and the improvement in the heliostat orientation accuracy to be verified.

Tab. 4: R-vector results and error percentage for heliostats with azimuth correction.

Instant	Time	Heliostat 1 (20cm x 20cm)		Heliostat 2 (30cm x 30cm)	
		Vector R (X, Y, Z)	Error	Vector R (X, Y, Z)	Error
1	11:20	[0.8306, 0.1003, 0.5477]	2.85°	[0.8046, -0.1654, 0.5702]	5.73°
2	11:30	[0.8338, 0.1015, 0.5427]	2.50°	[0.7757, -0.0680, 0.6275]	8.42°
3	11:40	[0.8324, 0.1019, 0.5447]	2.64°	[0.7720, -0.0851, 0.6299]	8.47°
4	11:50	[0.8347, 0.1084, 0.5399]	2.34°	[0.7653, -0.0764, 0.6391]	9.19°
5	12:00	[0.8323, 0.1061, 0.5441]	2.61°	[0.7908, -0.0956, 0.6046]	6.61°
6	12:10	[0.8280, 0.1082, 0.5502]	3.04°	[0.8076, -0.0885, 0.5831]	5.11°
7	12:20	[0.8321, 0.1128, 0.5430]	2.60°	[0.8041, -0.1010, 0.5859]	5.28°
8	12:30	[0.8260, 0.1159, 0.5516]	3.23°	[0.7850, -0.1015, 0.6111]	7.08°
9	12:40	[0.8308, 0.1022, 0.5471]	2.80°	[0.7814, -0.1036, 0.6154]	7.41°
10	12:50	[0.8322, 0.1071, 0.5441]	2.62°	[0.7718, -0.1230, 0.6239]	8.19°
11	13:00	[0.8341, 0.0933, 0.5436]	2.61°	[0.7759, -0.0990, 0.6230]	7.95°
12	13:10	[0.8529, 0.0790, 0.5160]	1.59°	[0.7652, -0.1782, 0.6186]	9.16°
13	13:20	[0.8421, 0.0839, 0.5327]	2.12°	[0.7972, -0.0922, 0.5967]	6.05°
14	13:30	[0.8487, 0.0972, 0.5199]	1.03°	[0.7927, -0.0578, 0.6068]	7.15°
		avg	2.47°	avg	7.27°

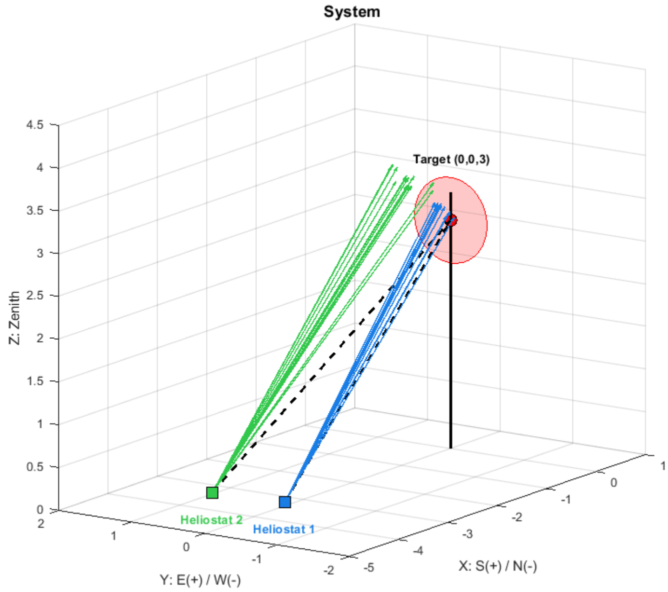

Fig. 10: Vectors from both heliostats with azimuth correction.

7. Conclusions and Future Work

Based on the comparative analysis between the two prototypes, it was demonstrated that the 20cm x 20cm design provides a significant improvement in solar tracking accuracy. The experimental vector analysis revealed that the new design (Heliostat 1) achieved an average angular error of 2.55°, significantly outperforming the 8.59° average error observed in the initial 30cm x 30cm prototype. This improvement was corroborated by the cross-validation between the experimental data and TracePro simulations, which showed an average calculated elevation error of just 1.14% for Heliostat 1, compared to 3.49% for the initial design. Similarly, the average azimuthal deviation ($\Delta\gamma_{AVG}$) was drastically reduced from 4.10° to 0.65°. The analysis of the target yielded an approximate concentrated irradiance of 1.9 W/m², with the cosine factor preventing the system from reaching the ideal 2 suns.

By aligning the mirror's centroid collinearly with the azimuthal and elevational axes of rotation, the mechanical deviations present in the initial prototype were successfully mitigated. However, the cross-validation also confirmed an azimuthal offset associated with a misalignment of the heliostats relative to the East-West axis. With the application of an azimuth correction, the angular errors are reduced to 2.47° and 7.27°.

A persistent behavior was observed in both devices: the experimental elevation required to focus the light beam onto the center of the receiver was consistently higher than the simulated value. This phenomenon is attributed to a vertical leveling offset at the base of the prototypes, potentially caused by the roof surface. To build upon these findings, future work will focus on strictly correcting these structural and leveling misalignments during the physical installation phase to enable fully autonomous operation.

Furthermore, the integration of the camera-based shadow analysis methodology will be prioritized. By implementing this computer vision approach, the system will bypass the need for manual calibration, dynamically extracting the real-time solar vector to establish a completely closed-loop, automated tracking network. Ultimately, refining the optical and mechanical precision of these small-scale, modular heliostats provides a scalable and cost-effective framework to support high-temperature SHIP applications, thereby contributing to the broader industrial energy transition.

References

AEE INTEC. Database of solar heat applications in industrial processes. https://ship-plants.info/, 2026. Accessed: 2026-08-03.

F. Cock Martínez. Diseño mecánico de un heliostato modular. Master's thesis, Centro de Investigaciones en Óptica A.C., León, Guanajuato, México, 2018. https://cio.repositorioinstitucional.mx/jspui/bitstream/1002/641/1/17354.pdf.

European Heat Pump Association (EHPA). Heat pumps for industry. https://hp4industry.ehpa.org/, 2026. Accessed: 2026-07-20.

Eurostat. Final energy consumption in industry - detailed statistics. European Commission, 2024. URL https://ec.europa.eu/eurostat/statistics-explained/index.php?title=Final_energy_consumption_in_industry_-_detailed_statistics. Accessed: 2026-08-08.

L. Kumar, M. Hasanuzzaman, and N. A. Rahim. Global advancement of solar thermal energy technologies for industrial process heat and its future prospects: A review. *Energy Conversion and Management*, 195: 885–908, 2019. doi: 10.1016/j.enconman.2019.05.081.

Osama A. Marzouk. Solar heat for industrial processes (SHIP): An overview of its categories and a review of its recent progress. *Solar*, 5:46, 2025. doi: 10.3390/solar5040046.

Job Ordaz-Castillo, Héctor D. García-Lara, Santos Méndez-Díaz, Oscar A. de la Garza, and Simón Martínez-Martínez. Design and validation of a passive solar tracking sensor based on gnomon shadow analysis. *International Journal of Photoenergy*, 2026(1):8110694, 2026. doi: https://doi.org/10.1155/ijph/8110694. URL https://onlinelibrary.wiley.com/doi/abs/10.1155/ijph/8110694.

Ibrahim Reda and Afshin Andreas. Solar position algorithm for solar radiation applications. Technical Report NREL/TP-560-34302, National Renewable Energy Laboratory (NREL), Golden, CO, January 2004. https://www.nrel.gov/docs/fy04osti/34302.pdf.

Secretaría de Energía (SENER). Balance nacional de energía 2023. Technical report, Gobierno de México, Ciudad de México, México, 2023. URL https://www.gob.mx/cms/uploads/attachment/file/977268/Balance_Nacional_de_Energ_a_2023.FINAL06.02.2025.1.pdf.

Secretaría de Energía (SENER). Balance nacional de energía 2024. Technical report, Gobierno de México, Ciudad de México, México, 2024. URL https://www.gob.mx/cms/uploads/attachment/file/1047704/Balance_Nacional_de_Energ_a_2024R.pdf.

Solar Heat Europe. Solar thermal in europe. https://solarheateurope.eu/, 2026. Accessed: 2026-07-20.

Solar Payback. Solar heat for industry: Solar payback. Technical report, International Climate Initiative (IKI), Federal Ministry for the Environment, Nature Conservation, Building and Nuclear Safety, Berlin, Germany, 2017.